THE JOURNAL OF PHYSICAL CHEMISTRY C

Article

pubs.acs.org/JPCC

Defect Chemistry of Ceria Nanorods

S. Agarwal,[†] X. Zhu,[‡] E. J. M. Hensen,[‡] L. Lefferts,[†] and B. L. Mojet*[,†]

[†]Catalytic Processes and Materials, MESA+ Institute for Nanotechnology, Faculty of Science and Technology, University of Twente, P.O. Box 217, 7500 AE Enschede, The Netherlands

[‡]Schuit Institute of Catalysis, Laboratory of Inorganic Materials Chemistry, Department of Chemical Engineering and Chemistry, Eindhoven University of Technology, P.O. Box 513, 5600 MB Eindhoven, The Netherlands

Supporting Information

ABSTRACT: Ceria nanorods were investigated using in situ Raman and FTIR spectroscopies for CO adsorption and subsequent reaction with water at 200 and 350 °C. The involvement of defects in ceria nanorods during CO adsorption and reaction with H_2O is dependent on the temperature. At 200 °C, most of the carbonate and formate species formed in CO do not involve the formation of defects, while at 350 °C all of the carbonates and formates formed can be correlated to the formation of defects (15% by formates and 85% by mono/bidentate carbonates). Finally, at 350 °C very stable polydentate carbonates are formed that do not induce defects and cannot be regenerated with water.

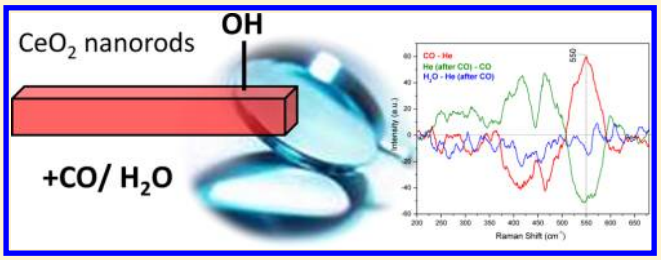

INTRODUCTION

Cerium oxide (CeO_2) is widely investigated as a catalyst or catalyst support for various applications in the field of environmental catalysis,[1] in three-way catalysts,[2] and as a catalyst support in heterogeneous catalysis.[3−9] The high performance of ceria is generally attributed to its unique redox nature and high oxygen storage capacity (OSC), allowing it to quickly switch its oxidation state between Ce^{4+} and Ce^{3+} in the stable fluorite structure.[10,11]

Due to recent advancement in synthesis approaches, ceria can now be synthesized into desirable nanoshapes with well-defined active exposed planes that further enhance the catalytic activity.[12,13] CeO_2 nanorods are an example of such tailored morphologies. In our recent work, we have reported that our ceria nanorods expose mainly (111) stable planes in place of the previously believed (110) and (100) planes.[14] As ceria nanorods provide a high surface area and have inherent defects (vacancy clusters, pits, and a high degree of surface roughness),[6,15] they are reported to have enhanced reactivity for the CO[10] and NO[16] oxidation and reduction reactions, respectively. One of the first detailed investigations of defects using UV (325 nm) Raman spectroscopy on these ceria nanoshapes was reported by Wu et al.[17] The authors showed that nanorods contain more intrinsic defect sites in comparison to other ceria nanoshapes (cubes and octahedra). Recently, Lee et al. reported about CO oxidation on ceria nanorods (with/without Au) by monitoring the oxygen vacancy levels using visible (514 nm) Raman spectroscopy.[18]

UV Raman spectroscopy is a potentially powerful tool to detect structural features, such as defect sites, oxygen vacancies, and atomic scale structure disorder of ceria nanomaterials.[19] In comparison to visible lasers, the use of UV lasers enhances the detection sensitivity in the surface region of these materials due to the limited probing depth of 10−20 nm.[20]

Despite the intensive studies of CO adsorption and H_2O reactivity on ceria supports, there is still a lack of understanding of the role of defects and active −OH species on ceria catalysts.[11,17,21−23] In our recent work, we investigated the reactivity of −OH species toward CO for different ceria nanoshapes at 200 °C.[24] We reported that the interaction of −OH groups with CO depends on the shape of ceria nanoparticles, and we showed preliminary data describing the importance of intrinsic defects in the ceria structure. Furthermore, theoretical investigations have clearly indicated that the formation of carbonate species induces defects in the ceria lattice upon interaction with CO.[43,54] In the present work, we follow up this by addressing the role of defects in ceria in detail using in situ UV Raman spectroscopy and the results will be related to Fourier transform infrared (FTIR) measurements recorded under similar conditions. This combination of techniques has proven successful in monitoring the structural defects and adsorbates on catalysts[8,55,56] We will assume that the concentration of defects at the surface is correlated with the bulk defect concentration which can be probed by Raman spectroscopy. We focus in this work on ceria nanorods due to their high intrinsic defect density as outlined above.

EXPERIMENTAL METHODS

Sample Preparation, HRTEM, and BET Characterization. Ceria nanorods were synthesized using the recipe

Received: October 8, 2013
Revised: February 3, 2014
Published: February 3, 2014

   dx.doi.org/10.1021/jp409989y | J. Phys. Chem. C 2014, 118, 4131−4142

reported by Mai et al.[13] For synthesis procedure details refer to the literature.[14] After drying, the sample was always calcined in air at 500 °C and subsequently analyzed using Raman and FTIR spectroscopies.

The X-ray diffraction (XRD) pattern of nanorods (not shown here) was similar to those reported in our previous work.[14] As reported earlier, the observed XRD diffraction peaks can be indexed as face-centered-cubic phase CeO_2.

A Micromeritics Tristar instrument was used for determining the BET surface area. The sample was outgassed in a vacuum at 300 °C for 24 h prior to N_2 physisorption. The BET surface area of the nanorods after calcination was 80 m^2/g, which is consistent with the values reported earlier.[17]

The high resolution transmission electron microscopic (HRTEM) image of the ceria rods was recorded on a GATAN CM300ST-FEG electron microscope (operated at an acceleration voltage of 300 kV). For HRTEM measurements, the sample was ultrasonically dispersed in ethanol and subsequently droplets of the suspension were deposited on a copper grid coated with carbon. The HRTEM image of ceria nanorods is shown in the Supporting Information (Figure S1). The low magnification HRTEM image of ceria nanorods demonstrates that the particles have the desired morphologies with a length of approximately 50−200 nm.

UV Raman Spectroscopy. UV Raman spectra (wavenumber region from 190 to 1480 cm^{-1}) were collected using a Jobin-Yvon T64000 triple-stage spectrograph with a CCD detector and a spectral resolution of 2 cm^{-1}. The laser spot size on the sample was less than 0.5 mm. The laser power at the sample was 6 mW for the 325 nm laser line of a Kinmon He−Cd laser. It was verified by recording spectra at different laser intensities that at these settings the laser did not induce any damage to the sample. The spectrum was recorded by two times 600 s subsequent laser exposure (two coadditions); hence recording per spectrum took 1200 s. Teflon was used as a standard for the calibration of the Raman shift. Typically, approximately 10 mg of sample was loaded and slightly compressed to get a dense catalyst bed in a purpose-built stainless steel in situ cell fitted with a thermocouple placed close to the sample. The cell was covered with a quartz assembly. The gas flows used in the in situ Raman experiments were preheated at 100 °C and then flowed through the sample. For CO adsorption experiments, 33 vol % CO (Linde) in He (Linde, total flow 20 mL/min) was used. For the H_2O reactivity measurements, He (20 mL/min) was flowed through a saturator filled with H_2O at 5 °C, resulting in a water vapor pressure of 9 mbar.

FTIR (Fourier Transform Infrared) Spectroscopy. Transmission FTIR measurements were recorded with a Bruker Vector 22 with an MCT detector by averaging 128 scans with a spectral resolution of 4 cm^{-1} and time interval of 120 s. The spectrum was collected in the wavenumber region 800−4000 cm^{-1}. A self-supporting wafer (≈10 mg sample) was pressed and placed into a custom-built stainless steel cell walled by the thermocouple. For adsorption experiments, 33 vol % CO in He (Hoekloos 4.7, total flow 20 mL/min) was used. For the water reactivity measurements, He (Hoekloos 5.0, total flow 20 mL/min) was flowed through a saturator filled with H_2O at 5 °C (H_2O vapor pressure of 9 mbar). All the tubings prior to the FTIR cell were heated to 100 °C, to avoid condensation of H_2O in the lines. To remove traces of water in He gas during FTIR experiments, helium was dried with a Varian Chromopack CP17971 gas clean moisture filter. The background spectrum was obtained while flowing He gas through an empty cell at room temperature.

Experimental Sequence. Raman and FTIR spectra were recorded after flowing gases in the sequence as shown in the experimental scheme in Figure 1. The sample was exposed to

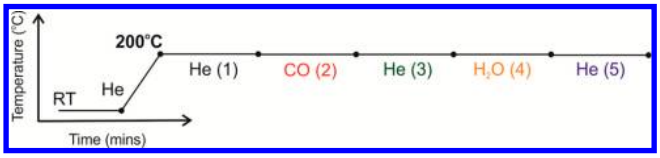

Figure 1. Experimental scheme for Raman and FTIR experiments at 200 and 350 °C.

each gas for 30 min respectively. The sample was heated to the required temperature (350 °C/200 °C) with a ramp rate of 5 °C/min. The total gas flow was maintained at 20 mL/min. We labeled each separate gas flow stage of the experimental sequence with its sequential number as indicated in Figure 1, which we use in the Results and Discussion section for clarity.

Data Analysis. Raman and FTIR data were analyzed using Bruker OPUS (version 7.0) software. All Raman spectra shown in the present paper were baseline corrected (concave rubber band correction, two iterations) and smoothened (using the OPUS Savitzky-Golay algorithm, 21 points) to better identify the observed changes. To verify that changes observed after smoothening are real, Figures S2 and S3 (see the Supporting Information) compare the raw and smoothened spectra. Raman spectra in Figure 2 were normalized with respect to the F2G band at 460 cm^{-1}. This is in accordance with common practice, although Daniel et al. have also employed the 2LO band (at 1179 cm^{-1}) for normalization.[59] The FTIR spectra presented in this work were baseline corrected (concave rubber band correction, two iterations).

To highlight the relative differences in the Raman and FTIR spectra as a function of gas treatment, the difference spectra in Figures 7 and 8 are expressed as the relative difference, defined as

$$y = \frac{\Delta I}{\Delta(I_{CO} - I_{He})}$$

where ΔI is defined as the difference between two consecutive treatments in the scheme shown in Figure 1. $\Delta(I_{CO} - I_{He})$ is the maximum peak intensity increase after dosing CO, at approximately 550 cm^{-1} for Raman and 1576 cm^{-1} for FTIR spectra, representing the total amount of species formed upon CO exposure. In addition, the relative amounts of species are calculated by integrating the specific peaks observed in normalized Raman and FTIR plots (see Figures 7 and 8). By expressing both the Raman and FTIR changes in relative differences, the observed changes by the two techniques can be easily compared.

RESULTS AND DISCUSSION

In Situ Raman and FTIR Spectra in Helium at Room Temperature (RT). In situ Raman and FTIR spectra of the fresh ceria nanorod samples in He flow at room temperature are shown in parts a and b, respectively, of Figure 2. The Raman spectra were normalized to the 460 cm^{-1} peak. The Raman spectrum of the calcined ceria nanorods (Figure 2a) consisted of sharp peaks at 460 and 589 cm^{-1}, shoulder peaks at 404 and 487 cm^{-1} and a broad intense band at 1179 cm^{-1}. The

dx.doi.org/10.1021/jp409989y | J. Phys. Chem. C 2014, 118, 4131−4142

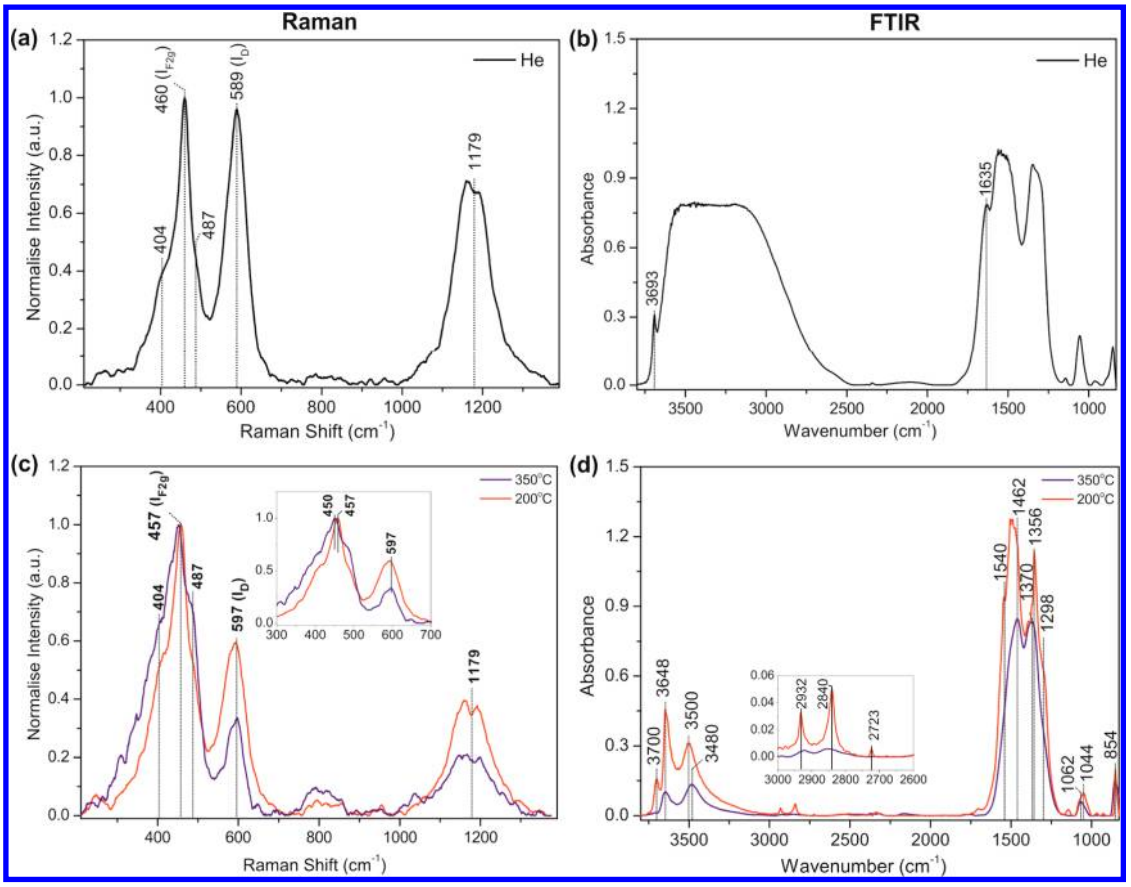

Figure 2. In situ (a) normalized Raman and (b) FTIR spectra of ceria nanorods in He flow at room temperature (black spectrum). In situ (c) Raman and (d) FTIR spectra of ceria rod in He flow at 200 (red spectrum) and 350 °C (blue spectrum).

peak at 460 cm^{-1} (labeled as I_{F2g}) is due to the symmetric stretch mode of the Ce−O_8 crystal unit, which is characteristic for the fluorite lattice structure.[25,26] In addition, the peak at 589 cm^{-1} (I_D) has been assigned to the defect-induced mode arising due to the presence of Frenkel-type anion defects (an oxygen ion is displaced from its lattice position to an interstitial position, creating a vacancy at its original position and a defect at the interstitial site) in the ceria lattice.[17,20,26,27] Shoulder peaks at 404 and 487 cm^{-1} on both sides of the fluorite band have been earlier observed for ceria nanoparticles,[17,28] although they were not assigned. The band centered at 1179 cm^{-1} corresponds to the second overtone of the longitudinal optical (LO) band.[20,26,29]

In Figure 2b, the FTIR spectrum of fresh ceria nanorods was dominated by the strong bands related to physisorbed water in the spectral region 3800−2500 cm^{-1} and at 1635 cm^{-1}.[30] Other than these physisorbed water bands, ceria hydroxyl (O−H) stretching vibrations at 3693 cm^{-1} and formate and carbonate (C−O) stretching and deformation bands between 1700 and 800 cm^{-1} were observed.[31−33] These carbonate/formate species formed due to the interaction of lattice oxygen/hydroxyl species with atmospheric CO_2 on the fresh ceria sample when exposed to air.[34,35]

In Situ Raman and FTIR Spectra in Helium at 200 and 350 °C. In situ normalized Raman spectra of calcined ceria nanorods in He flow at temperatures 200 and 350 °C are shown in Figure 2c. Similar to the Raman spectrum at room temperature, the fluorite lattice vibration I_{F2g} (457 cm^{-1}) and I_D defect band (597 cm^{-1}) were observed at 200 and 350 °C (Figure 2c). Two immediate observations related to the fluorite band can be made: First, the peak at 460 cm^{-1} (RT) shifted to 457 cm^{-1} (200 °C) and then to 450 cm^{-1} (350 °C). Second, the relative intensity of the shoulder fluorite peaks at 404 and 487 cm^{-1} increased with temperature, resulting in an overall broad fluorite band centered 450 cm^{-1} at 350 °C. The relative intensities of the peaks at 597 and 1179 cm^{-1} with respect to the I_{F2g} vibration decreased with temperature. We further observed an as yet unreported small overall shift from 589 to 597 cm^{-1}.

As reported previously, the broad fluorite band observed in the Raman spectra (Figure 2) and the broad XRD peaks (as compared to other ceria nanoshapes) reported earlier[17,24] are due to the distorted fluorite structure of ceria nanorods. This lattice distortion occurs due to the presence of intrinsic roughness (internal voids and surface steps) in nanorods.[6,15] We propose that the distortion in the lattice gives rise to bands at 404 and 487 cm^{-1} in ceria nanorods. At higher temperature, oxygen mobility is enhanced leading to reorganization of the ceria lattice.[36] This explains the decrease in I_D intensity with an increase in Ce−O vibration intensity (I_{F2g}) with the increase in intensities of the side peaks at 404 and 487 cm^{-1}, as observed in Figure 2c. Any further shift or broadening of I_{F2g},[18,37] or possible shift of the I_D peak, can be attributed to thermal restructuring, i.e., the recombination of defects with vacant lattice sites.

In situ transmission FTIR spectra of ceria nanorods obtained in helium flow at 200 and 350 °C are shown in Figure 2d. As is clearly evident, the strong bands corresponding to physisorbed water that were present at RT (Figure 2b) disappeared, leaving

dx.doi.org/10.1021/jp409989y | J. Phys. Chem. C 2014, 118, 4131−4142

behind distinct peaks in the O−H stretching range between 3800 and 3000 cm^{-1}.

At 200 °C there are three clear regions, corresponding to hydroxyl, formate, and carbonate species. The hydroxyl stretch regions for nanorods showed three strong bands at 3700, 3648, and approximately 3500 cm^{-1}, corresponding to single-coordinated hydroxyl species, bridging hydroxyls, and hydrogen bonded −OH species, respectively.[5,31,34,38] The peaks observed at 2932, 2840, and 2723 cm^{-1} are assigned to C−H stretching vibrations of formate species.[38−40] Finally, between 1800 and 800 cm^{-1}, intense bands were observed related to C−O stretching and bending vibrations of carbonates (visible at 1356 and 854 cm^{-1}) and formates (evident from peak at 1540 cm^{-1}, see also Figure S10 in the Supporting Information).[24,41] Based on the literature, several carbonate species can be distinguished in the 1800−800 cm^{-1} range; see Figure 3 and Table 1 for structures and the peak assignments.

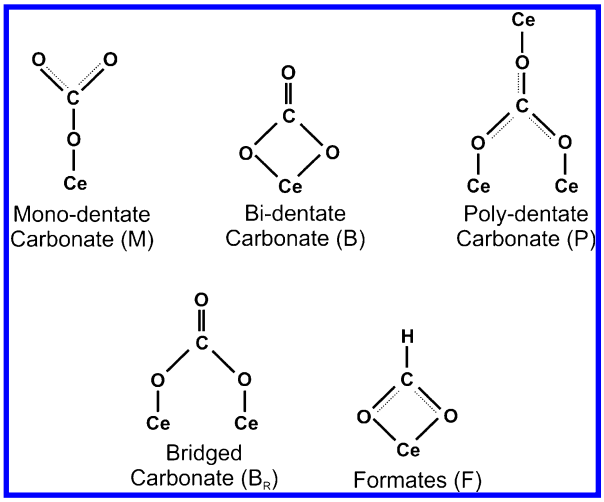

Figure 3. Schematic of types of carbonate and formate species.

Table 1. FTIR Peak Assignments of Carbonate and Formate Species Observed on Fresh Ceria Nanorods at 200 and 350 °C[a]

peak (cm^{-1})	type of species	temp (°C)	ref
2932	F + second overtone of P	200	38−41
2922	second overtone of P	350	38
2840	F + second overtone of P	200	38−41
2850	second overtone of P	350	38
2723	F	200	38−40
1540	F	200	38−41
1494	M	200	32, 35, 46
1474	B	200	32, 47
1462	P	200, 350	32, 35, 38
1391	B_R	200	32, 38
1370	P	200, 350	32, 35, 38, 41
1356	M	200	32, 35, 38, 41, 46
1298	F	200	32, 38−41
1145	B_R	200	32, 38
1062	P	200, 350	35, 38, 41
1044	M	200	32, 41, 46
854	M, B, and P	200	32, 35, 38, 41
854	P	350	35, 38, 41

[a] F, formates; P, polydentate carbonates; M, monodentate carbonates; B, bidentate carbonates; B_R, bridged carbonates.

As can be seen in Figure 2d, formate (1540 and 1298 cm^{-1}) and mono/bidentate carbonates (1044/1474 cm^{-1}) species were no longer visible as they are unstable at 350 °C.[40] As a result, two distinct regions related to hydroxyl and carbonate bands were observed. In comparison to 200 °C, at 350 °C total hydroxyl peak intensities in region 3800−3000 cm^{-1} were lower. In addition, the 3700 cm^{-1} band disappeared and the 3648 cm^{-1} peak decreased in intensity relative to that at 3500 cm^{-1}. The carbonate peaks observed in the region 1600−800 cm^{-1} (see Table 1 for peak assignments) correspond to polydentate species (see Figure 3).[35]

At 350 °C, fewer carbonate species were observed with FTIR spectroscopy compared to 200 °C, accompanied by the decrease in the peak ratio $I_{D/F2g}$ in Raman spectra. It is reported in the literature that exposure of ceria to CO/CO_2 results in the formation of carbonates by interaction with lattice oxygen, which creates defects in the ceria lattice.[42−45] The presence of fewer carbonate species (observed via FTIR spectroscopy) hence also explains the existence of fewer defects ($I_{D/F2g}$, Raman spectroscopy) at 350 °C. More details on the relation between defects and carbonate species are discussed below.

In Situ Raman Spectroscopy at 200 °C: CO Adsorption and H_2O Reactivity. To investigate the defect chemistry of ceria nanorods at 200 °C, the sample was exposed to the series of gas flows outlined in Figure 1, resulting in the spectra shown in Figure 4. Running from top to bottom of Figure 4, each plot on the left-hand side contains two spectra corresponding to "before" and "after" exposure to the respective gas flow. The graphs plotted in the right-hand column are the *difference spectra* of the spectra in the left column. The difference spectra were obtained by subtracting the spectrum obtained before exposure from the spectrum obtained after exposure.

In Figure 4a, the spectrum obtained in CO (2) flow at 200 °C is shown together with the spectrum in He flow (He (1)). To focus on the Raman intensities of fluorite and defect bands under exposure to CO and H_2O, the spectral region 200−680 cm^{-1} is shown. In CO, the broad fluorite band centered at 457 cm^{-1} decreased in intensity as is evident from the negative peaks at 413 and 464 cm^{-1} in the difference spectrum (Figure 4b). The overall I_D band (520−590 cm^{-1}) broadened to a lower wavenumber due to a new band arising at 550 cm^{-1}, clear from the difference spectrum (2) − (1) in Figure 4b. The maximum intensity of the defect peak at 593 cm^{-1} remained unchanged. This observation indicates the formation of defects in the ceria lattice upon introduction of CO, which is in agreement with the literature.[8,18,43] The inverse relation between the I_{F2g} lattice vibration and the defect I_D band has been suggested previously in the literature.[18]

The spectrum in CO (2), the spectrum obtained in He (3) immediately after CO, and their difference are shown in Figure 4c,d. On flowing He (3), 95% changes that were observed upon CO introduction disappeared and the spectrum regained its original peak positions as for the fresh sample in He (1). This observation indicates that the CO-induced changes are reversible on the ceria rods at 200 °C.

H_2O/He (4) was flowed after He (3); see Figure S4 in Supporting Information for the spectrum obtained after H_2O/He (4). Subsequently, He (5) was flowed to remove physisorbed H_2O, and the resulting spectrum is shown in Figure 4e. Only subtle changes in intensities of the fluorite peaks at 457 and 404 cm^{-1} and the defect band at 593 cm^{-1}

dx.doi.org/10.1021/jp409989y | J. Phys. Chem. C 2014, 118, 4131−4142

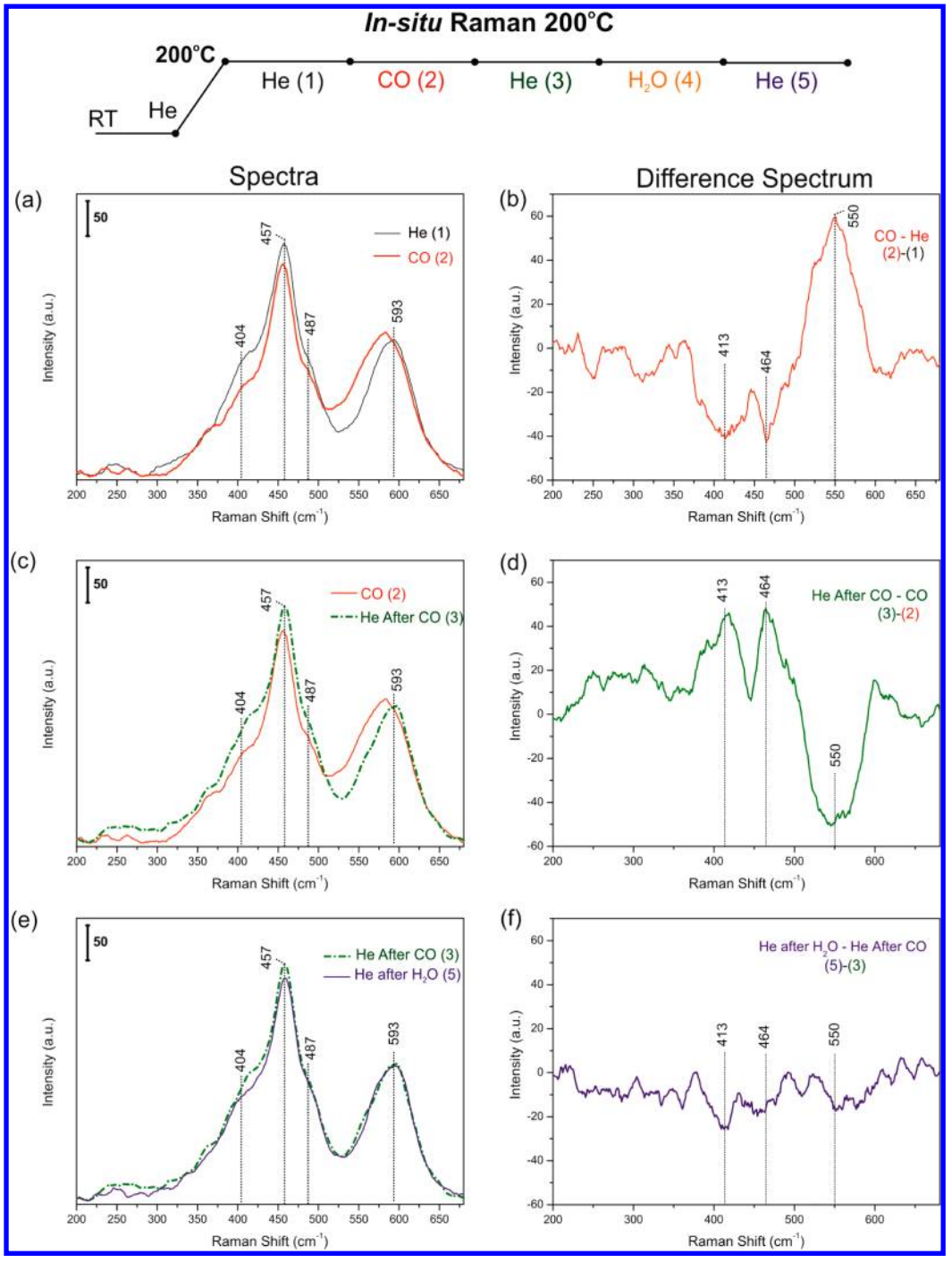

Figure 4. In situ Raman spectra at 200 °C of ceria nanorods (a) in He (1) (black spectrum), followed by CO (2) (red line); (b) CO (2)−He (1); (c) CO (2) (red line) followed by He (3) (green dash−dotted line); (d) He (3)−CO (2); (e) He (3) and He (5) after He/H_2O (4) flow (blue spectrum); (f) He (5)−He (3).

were observed upon water treatment and subsequent He flow as confirmed by the difference spectrum in Figure 4f.

In Situ Raman Spectroscopy at 350 °C: CO Adsorption and H_2O Reactivity. The Raman spectra for ceria nanorods at 350 °C after CO adsorption and rehydration with H_2O can be seen in Figure 5 (left-hand column). In the difference spectra shown in Figure 5 (right-hand column), the induced changes on adsorption of CO and regeneration by H_2O can be seen more specifically.

In Figure 5a, the spectrum obtained in CO (2) flow is plotted with the spectrum in He (1). In the presence of CO, decrease in intensity of the entire fluorite band (404, 450, and 487 cm^{-1} peaks combined) was observed. In addition, the defect peak at 597 cm^{-1} remained unchanged. The band between 520 and 590 cm^{-1} significantly increased due to the formation of additional new defect peaks at lower wavenumbers (see Figure 5b). Due to the noise level of the spectrum and thus the uncertainty in peak position, individual defect peaks were not specifically assigned in Figure 5. The spectrum obtained on flowing He (3) after CO can be seen in Figure 5c (green dash−dotted spectrum) together with the CO (2) spectrum. Minor changes were observed, i.e., a small increase in

dx.doi.org/10.1021/jp409989y | J. Phys. Chem. C 2014, 118, 4131−4142

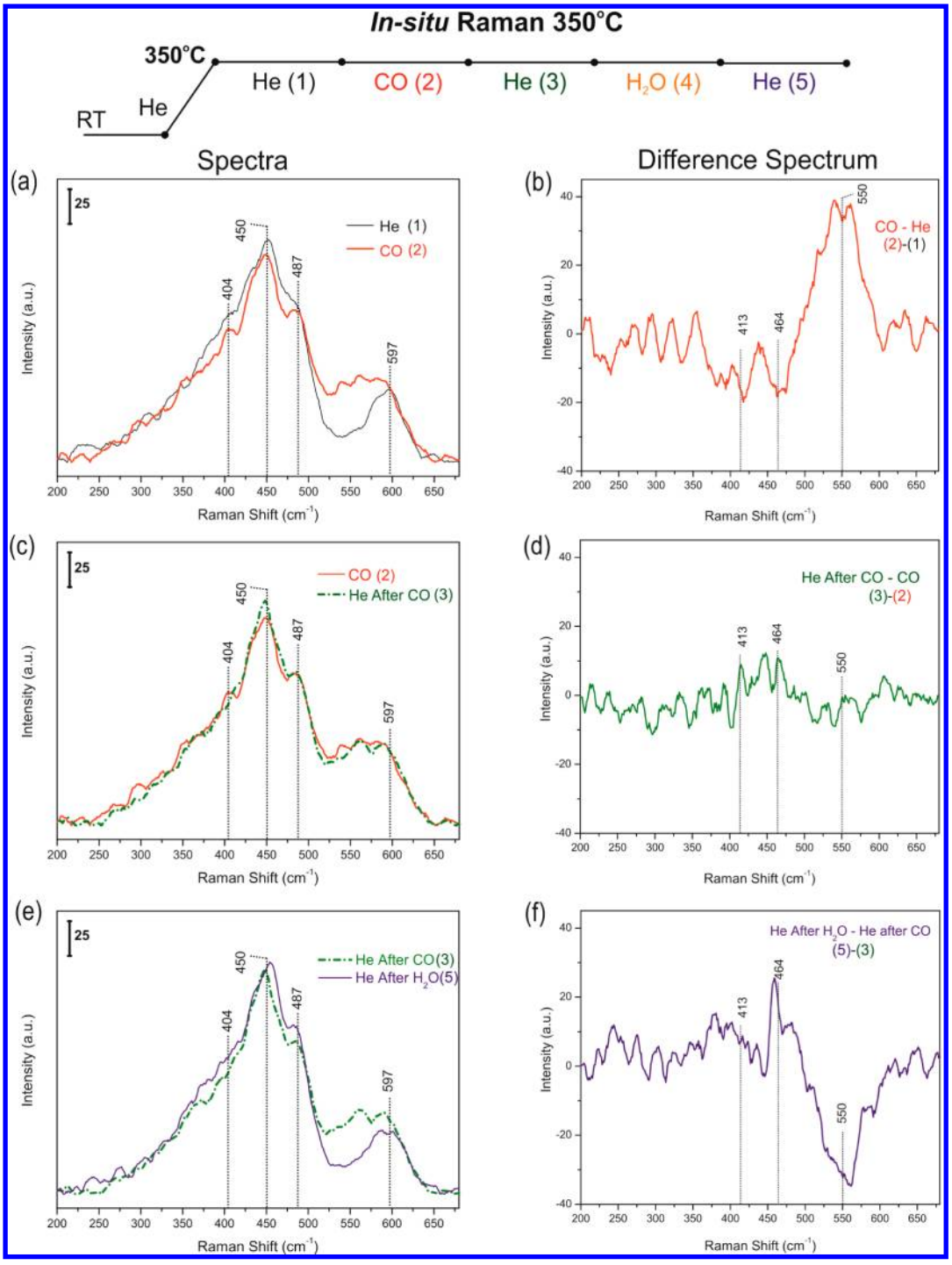

Figure 5. In situ Raman spectra at 350 °C of ceria nanorods (a) in He (1) (black spectrum), followed by CO (2) (red line); (b) CO (2)−He (1); (c) CO (2) (red line) followed by He (3) (green dash−dotted line); (d) He (3)−CO (2); (e) He (3) and He (5) after He/H_2O (4) flow (blue spectrum); (f) He (5)−He (3).

the intensity of the 450 cm^{-1} peak and a subtle decrease in the defect-related band, as can be better seen in the difference spectrum in Figure 5d.

Subsequently, the sample was exposed to H_2O/He (4) flow (Figure S5 in the Supporting Information) followed by He (5) to remove physisorbed water (Figure 5e). After exposure to H_2O and He (5), the fluorite band centered at 450 cm^{-1} showed an increased intensity accompanied by an overall band broadening. The CO-induced defect band centered at 550 cm^{-1} disappeared (Figure 5f), and thus the overall peak area of the defect band between 520 and 590 cm^{-1} decreased. As indicated above, the observations at 350 °C suggest that the I_D band is inversely connected to the I_{F2g} band.

It is clear from Raman spectra that the interaction of CO and subsequent reaction with H_2O on ceria nanorods is different at 200 °C compared to 350 °C. The differences are addressed in detail in the General Discussion section when compared to the changes observed in the infrared spectra.

In past years, several studies proposed different types of defects in ceria lattices, which can be classified into four

dx.doi.org/10.1021/jp409989y | J. Phys. Chem. C 2014, 118, 4131−4142

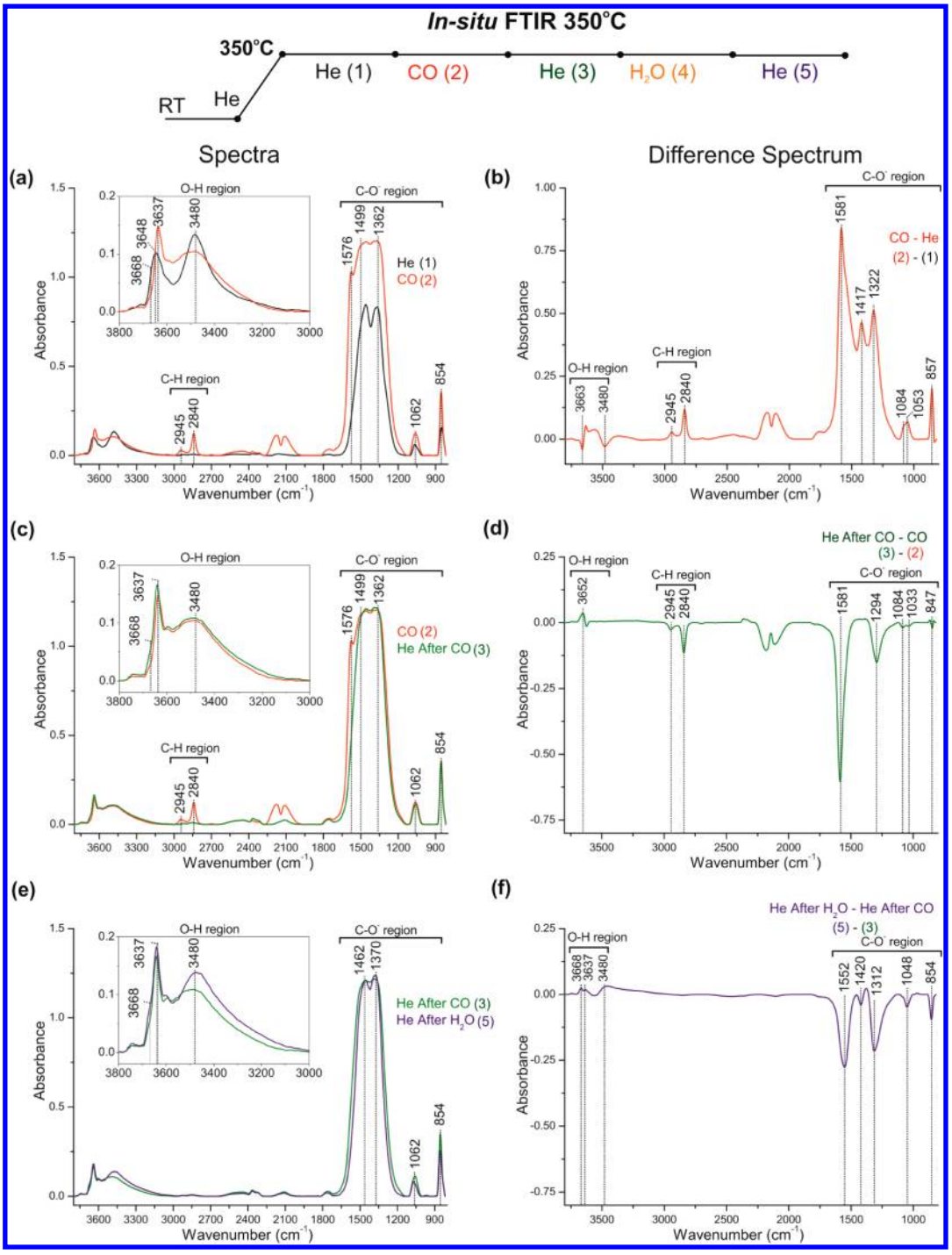

Figure 6. In situ FTIR spectra at 350 °C of ceria nanorods (a) in He (1) (black spectrum), followed by CO (2) (red line); (b) CO (2)−He (1); (c) CO (2) (red line) followed by He (3) (green dash−dotted line); (d) He (3)−CO (2); (e) He (3) and He (5) after He/H_2O (4) flow (blue spectrum); (f) He (5)−He (3).

different types based on energy calculations.[48−50] The four types are (1) anion Frenkel pairs (an oxygen atom is displaced from its lattice position to interstitial site), (2) oxygen vacancies (an oxygen atom is missing from one of the lattice positions), (3) interstitial sites (displacement of both a cerium and oxygen ion to interstitial sites), and (4) Schottky disorders (removal of cations and anions from their lattice sites creating vacancies while maintaining stoichiometry). In all cases, the formation of these defects introduces vacant sites (V) in the ceria lattice. Anion Frenkel pair defects (ca. 600 cm^{-1}) and oxygen vacancy defects (550 ± 10 cm^{-1}) were experimentally first assigned on doped ceria[20,51,52] and subsequently for uncalcined ceria nanoparticles.[37] For calcined ceria nanoshapes, Wu et al. suggested the presence of anion Frenkel pair defects, and showed that oxygen vacancy defects appear after H_2 treatment at 600 °C.[17]

In the present study, CO exposure to ceria nanorods results in the formation of a Raman band centered at 550 cm^{-1}, which could be assigned to oxygen vacancy defects based on previous assignments. However, the I_D band is very broad and has

dx.doi.org/10.1021/jp409989y | J. Phys. Chem. C 2014, 118, 4131−4142

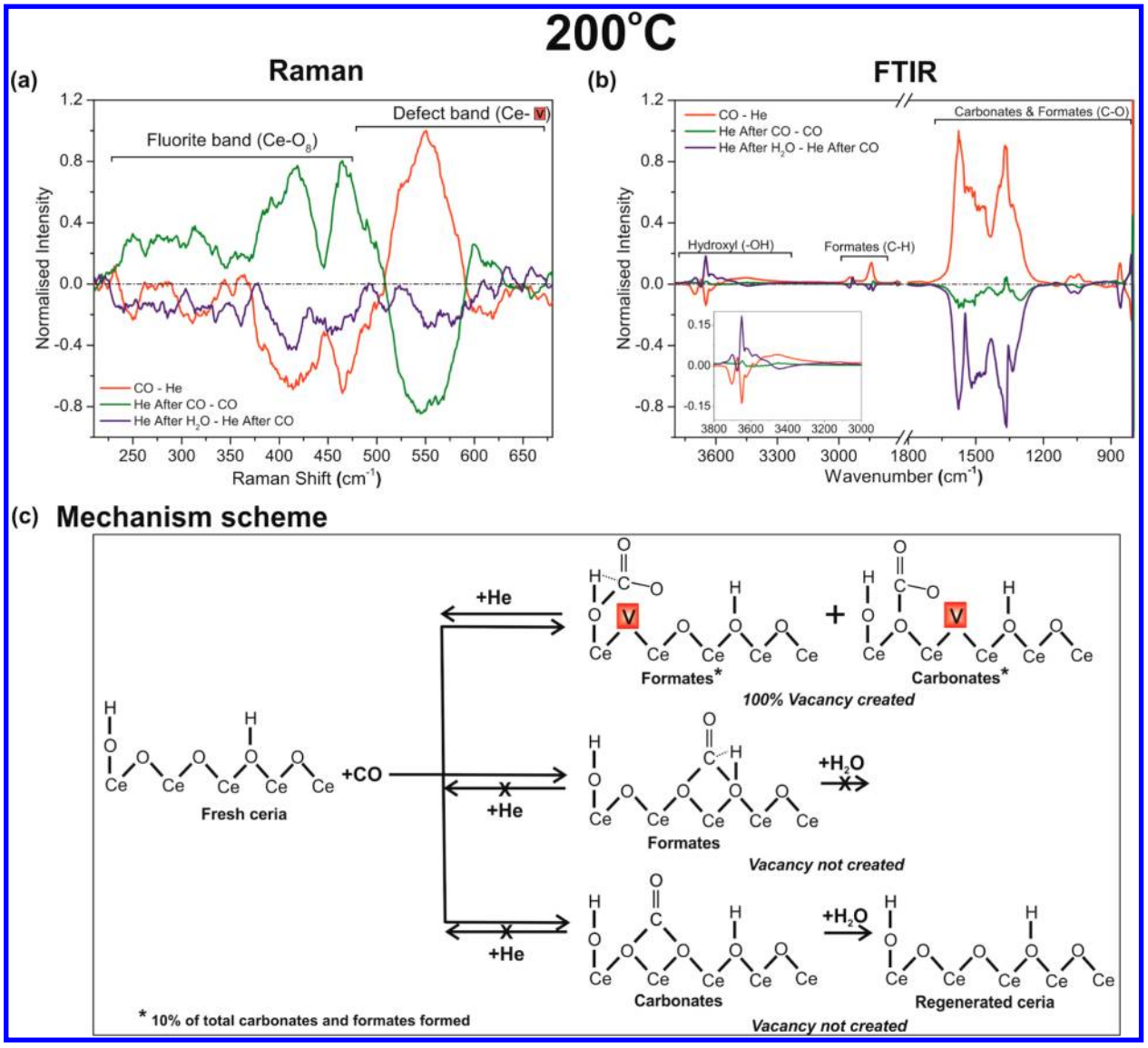

Figure 7. Relative changes introduced in different gases with respect to the species formed in CO for (a) Raman and (b) FTIR data at 200 °C. (c) Schematic reaction mechanism of ceria nanorods at 200 °C ("V" represents oxygen vacancy). For simplicity only surface defects are indicated. However, oxygen diffusion will occur through the lattice to reach equilibrium between surface and bulk defects.

distinct shoulder peaks at 525 and 570 cm^{-1} (Figure 4). In our opinion, the observation of these shoulders suggests the existence of different types of defects, such as interstitial defects and Schottky disorder, in addition to the previously proposed Frenkel pair defects, and can also be due to the clustering of vacancy defects to form vacancy dimers and trimers.[57,58] We believe that the present work is the first experimental evidence that shows the existence of additional types of defects. Further investigations are required for specific defect identification and corresponding peak assignment. In the remainder of this paper we will refer to vacancies (V) without differentiating between the different kinds of oxygen disorder in the ceria lattice.

In Situ FTIR Spectroscopy at 200 °C: CO Adsorption and H_2O Reactivity. Recently, we reported FTIR studies on ceria nanowires at 200 °C.[24] The spectral patterns when exposed to CO and H_2O at 200 °C for ceria nanorods obtained in this study are similar to those reported for ceria wires. To avoid duplication of results, the FTIR plots for the ceria nanorods are shown in Figure S6 in the Supporting Information. Summarizing, the following observations were made: On exposure to CO, the isolated −OH species (at 3700 and 3648 cm^{-1} in the Supporting Information, Figure S6) decreased in intensity accompanied by significant formation of formates (3000−2800, 1800−800 cm^{-1}) and carbonates (1800−800 cm^{-1}). Upon subsequent exposure to He after CO flow, approximately 10% of the adsorbed carbonate and formate species desorbed with subtle regeneration of bridging hydroxyl ($-OH^{3648}$) species. Finally, by flowing H_2O/He for 30 min, major regeneration of hydroxyl species and decomposition of carbonate and formate species (approximately 90%) occurred; Figure S11 in the Supporting Information presents a set of time-resolved spectra, showing that most of the changes take place in the first 5 min.

In Situ FTIR Spectroscopy at 350 °C: CO Adsorption and H_2O Reactivity. The in situ FTIR spectra at 350 °C are shown in Figure 6. Upon exposure to CO (2), the $-OH^{3668}$ and $-OH^{3480}$ intensities decreased, whereas the $-OH^{3648}$ peak increased and shifted to 3637 cm^{-1} (Figure 6a, inset). The latter band has been previously assigned to O−H stretching in

dx.doi.org/10.1021/jp409989y | J. Phys. Chem. C 2014, 118, 4131−4142

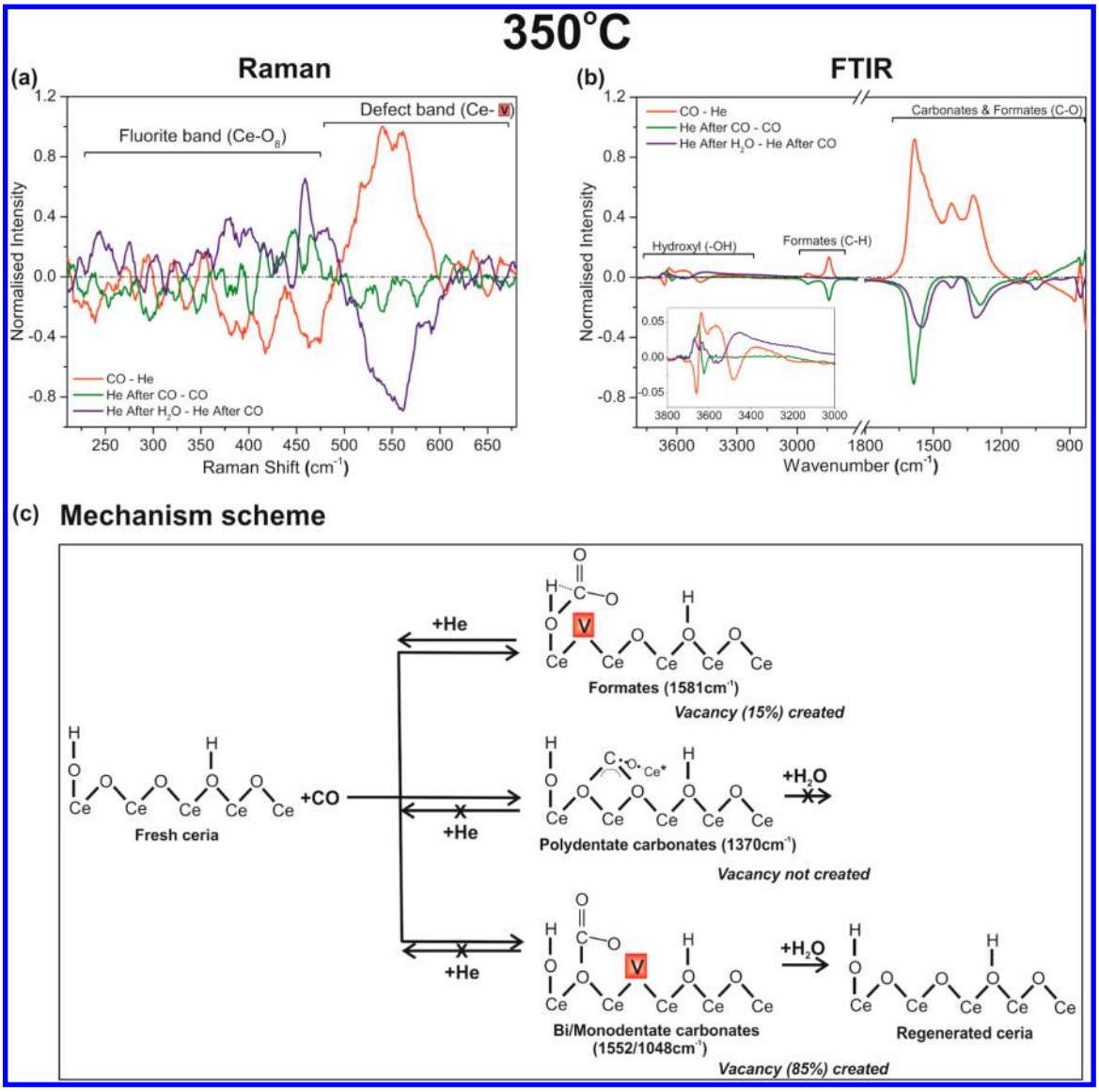

Figure 8. Relative changes introduced in different gases with respect to the species formed in CO for (a) Raman and (b) FTIR data at 350 °C. (c) Schematic reaction mechanism of ceria nanorods at 350 °C ("V" represents oxygen vacancy). For simplicity only surface defects are indicated. However, oxygen diffusion will occur through the lattice to reach equilibrium between surface and bulk defects.

$CO_2(OH)^-$.[38,53] In addition, the formation of formate C−H stretch bands at 2945 and 2840 cm^{-1} was observed, with a significant increase in peak intensity for C−O vibrations of formates and carbonates in the 1800−800 cm^{-1} region (see Figure 6a). The exact band positions of the species formed (at 1581, 1417, 1322, 1084, 1053, and 857 cm^{-1}) can be better seen in the difference spectrum (Figure 6b). After CO, the sample was exposed to He (3) (green spectrum in Figure 6c). The key observations were a slight rise in intensity of hydroxyl species at 3668 cm^{-1}, with an increase and shift of the 3637 cm^{-1} peak to a higher wavenumber (evident from the S-curve[3652] in the difference spectrum in Figure 6d). Furthermore, the formate peaks at 2945 and 2840 cm^{-1} disappeared and the band in the region 1800−1100 cm^{-1} became narrower. These induced changes are clearly visible in Figure 6d, where negative bands at 1581, 1294, 1084, 1033, and 847 cm^{-1} are observed.[41] The disappearance of C−H and C−O vibrations of formates in the difference spectrum indicates the decomposition of formate species.

On subsequent treatment with H_2O/He (4) followed by He (5) (blue spectrum in Figure 6e), −OH groups at 3668, 3637, and 3480 cm^{-1} were restored (Figure 6e, inset). Furthermore, subtle changes were observed in the carbonate region (1700−800 cm^{-1}). In the difference spectrum (Figure 6f), negative carbonate bands at 1552, 1420, 1312, 1048, and 854 cm^{-1} were observed, indicating decomposition of carbonate species. Based on the literature, these carbonate species were identified as bi/monodentate carbonates.[32,34,38] Therefore, the remaining carbonates in the spectrum (at 1462, 1370, 1062, and 854 cm^{-1}) after treatment with H_2O correspond to polydentate species (see Table 1).[41] These carbonates are also visible when comparing the spectra obtained at 350 °C for the fresh and regenerated nanorod samples (Supporting Information, Figure S8). The amount of −OH species (region 3800−3000 cm^{-1}) recovered after H_2O treatment was higher in comparison to that in the fresh sample.

dx.doi.org/10.1021/jp409989y | J. Phys. Chem. C 2014, 118, 4131−4142

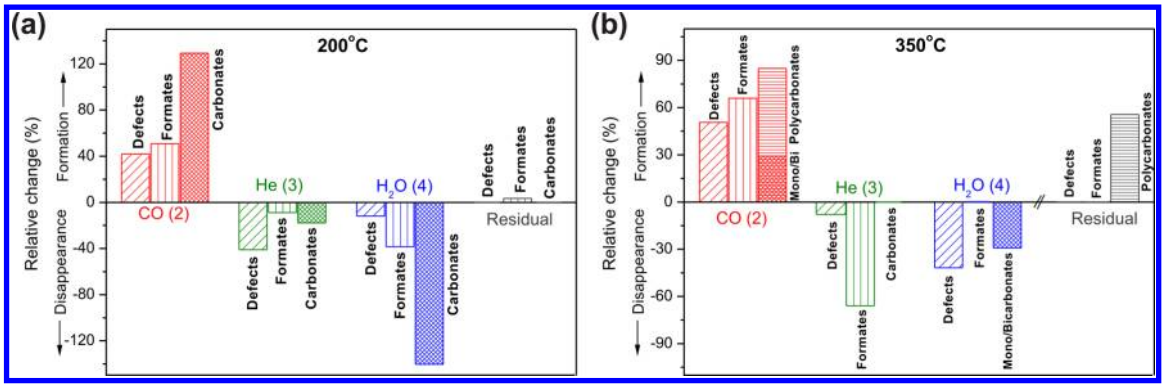

Figure 9. Bar diagram of species formed (positive) and decomposed (negative values) on introduction of different gases in ceria nanorods at 200 and 350 °C. The numbers represent the relative change (%) for each individual species.

GENERAL DISCUSSION

Ceria Nanorod Defect Chemistry at 200 °C. To compare the Raman and FTIR results, the relative differences in the Raman spectra were plotted with respect to the most intense defect peak (≈550 cm^{-1}) formed upon introduction of CO (see Experimental Methods). We have assumed that the total defect concentration is semiquantitatively correlated with the relative Raman intensities. Likewise, FTIR difference spectra were normalized with respect to the most intense peak (formate peak at approximately 1576 cm^{-1}). The relative changes observed on exposure to each gas type at 200 °C in both Raman and FTIR spectra are shown in parts a and b, respectively, of Figure 7.

The red spectra in Figure 7a,b show that with the formation of vacancies (Raman spectrum, 550 cm^{-1}) significant amounts of formates and carbonates are formed (FTIR spectrum, 1800−800 cm^{-1}). This observation is schematically represented in Figure 7c. Upon flowing He after CO, the majority of defects disappear (Figure 7a, green line). At the same time in the FTIR spectrum at 200 °C (Figure 7b, green line), only approximately 10% decomposition of formates and carbonates and 10% regeneration of −OH groups are observed. Thus, desorption at this stage indicates that the defects created are related to about 10% of the carbonates and formates formed on exposure to CO and that they are reversible in nature (schematically depicted in Figure 7c, top row). Separation of different types of carbonate species connected with defects is not possible for this experiment because they decompose simultaneously.

Finally, the FTIR spectra show that major regeneration of −OH species and decomposition of carbonates and formate species occur in the presence of H_2O (Figure 7b, blue line), without significant changes in the defects observed with Raman spectrscopy.

In conclusion, at 200 °C, upon the introduction of CO, 90% of the carbonate and formate species formed do not involve the creation of defects as depicted in Figure 7c (middle and bottom rows). Most of those species decompose in the presence of H_2O while regenerating the −OH groups.

Ceria Nanorod Defect Chemistry at 350 °C. The normalized Raman and FTIR plots obtained at 350 °C with the mechanism scheme are shown in Figure 8. Similar to the experiment at 200 °C, at 350 °C also formates and carbonates are formed by interaction of CO with −OH species, simultaneously creating defects in the ceria lattice (Figure 8c depicts a schematic representation).

Interestingly, subsequent He flush decomposes only all formates, most clearly evidenced by the negative peak for the C−H vibrations between 3100 and 2900 cm^{-1}. The complete formate decomposition only removes 15% of the vacancies (Figure 8a, green line), while recreating hydroxyl groups. Thus, formates are forming at the expense of part of the hydroxyl species, and creating a small amount of defects within the ceria structure (schematically shown in Figure 8c, top row).

Upon H_2O flow, the remaining 85% of the defects disappeared (blue line, Figure 8a), while 35% of the carbonates decomposed (blue line, Figure 8b) and hydroxyl groups were formed. These carbonate bands at 1552/1048 cm^{-1} can be specifically attributed to mono- and bidentate carbonate species, leaving the polydentate carbonates as residual species on the ceria, as summarized in Figure 8c.

As the defects produced upon addition of CO disappeared after the series of treatments, it must be concluded that the polydentate carbonate species are not related to defect creation (labeled as "Vacancy not created" in Figure 8c).

Figure 9 summarizes the temperature effect on the reactivity of ceria with CO and subsequently H_2O. In Figure 9 the relative amounts of species appearing and disappearing upon the different treatments are compared for the experiments at 200 and 350 °C. Clearly, after regeneration with H_2O, at 350 °C stable polydentate carbonate species were observed, while no residual carbonates were observed at 200 °C [Figure 9 (residual species)]. At the same time, this study shows that the formation of vacancies in ceria nanorods cannot uniquely be assigned to the formation of a specific species adsorbed on ceria. Further, although the Raman signatures of the defect band arising after addition of CO are very similar (Figure S9, Supporting Information), their chemical origin seems to be different since at 350 °C the addition of H_2O is needed to remove the vacancies, while at 200 °C the majority disappeared already in He flow.

This research is an important step forward to understanding the behavior of ceria nanorods toward the catalytic reactions involving CO and water. Furthermore, our results give scope for further theoretical and experimental work to understand the roles of different defects in ceria catalysts.

CONCLUSION

This study revealed the complex role of defects in ceria for reactions involving CO and H_2O. For ceria nanorods, the involvement of defects during CO adsorption and consecutive reaction with H_2O fundamentally changes with temperature. At 200 °C, most of the carbonate and formate species that form in

dx.doi.org/10.1021/jp409989y | J. Phys. Chem. C 2014, 118, 4131−4142

CO do not induce the formation of any defects in the lattice. However, at 350 °C, the formation of formate and carbonate (bi/monodentate) species does lead to defect formation. Further, very stable polydentate carbonates are formed exclusively at 350 °C without creating vacancies and these species are stable in water vapor. These results show that, depending on temperature, the formation of certain specific formate and carbonate surface species involves lattice oxygen from CeO_2 forming defects, whereas other species do not.

■ ASSOCIATED CONTENT

Supporting Information

TEM image; additional in situ Raman and FTIR spectra of ceria nanorods obtained at 200 and 350 °C. This material is available free of charge via the Internet at http://pubs.acs.org.

■ AUTHOR INFORMATION

Notes

The authors declare no competing financial interest.

■ ACKNOWLEDGMENTS

The research was financially supported by ADEM Innovation Lab (Project Number 30961318). The work was performed under the auspices of NIOK. The authors gratefully acknowledge M. A. Smithers for HRTEM imaging and Karin Altena-Schildkamp for BET measurements. We would like to thank Ruben Lubkemann and Bert Geerdink for technical assistance. The in situ Raman experiments were performed at Schuit Institute of Catalysis in the laboratory of Inorganic Materials Chemistry at Eindhoven University of Technology, The Netherlands.

■ REFERENCES

(1) Garcia, T.; Solsona, B.; Taylor, S. H. Nano-Crystalline Ceria Catalysts for the Abatement of Polycyclic Aromatic Hydrocarbons. *Catal. Lett.* **2005**, *105* (3−4), 183−189.

(2) Diwell, A. F.; Rajaram, R. R.; Shaw, H. A.; Truex, T. J.; Crucq, A. The Role of Ceria in Three-Way Catalysts. *Stud. Surf. Sci. Catal.* **1991**, *71*, 139−152.

(3) Gorte, R. J. Ceria in catalysis: From Automotive Applications to the Water-Gas Shift Reaction. *AIChE J.* **2010**, *56* (5), 1126−1135.

(4) Gorte, R. J.; Zhao, S. Studies of the Water-Gas-Shift Reaction with Ceria-Supported Precious Metals. *Catal. Today* **2005**, *104* (1), 18−24.

(5) Jacobs, G.; Patterson, P.; Williams, L.; Sparks, D.; Davis, B. Low Temperature Water-Gas Shift: Role of Pretreatment on Formation of Surface Carbonates and Formates. *Catal. Lett.* **2004**, *96* (1−2), 97−105.

(6) Liu, X.; Zhou, K.; Wang, L.; Wang, B.; Li, Y. Oxygen Vacancy Clusters Promoting Reducibility and Activity of Ceria Nanorods. *J. Am. Chem. Soc.* **2009**, *131* (9), 3140−3141.

(7) Trovarelli, A.; de Leitenburg, C.; Boaro, M.; Dolcetti, G. The Utilization of Ceria in Industrial Catalysis. *Catal. Today* **1999**, *50* (2), 353−367.

(8) Wu, Z.; Li, M.; Overbury, S. H. On the Structure Dependence of CO Oxidation over CeO_2 Nanocrystals with Well-Defined Surface Planes. *J. Catal.* **2012**, *285* (1), 61−73.

(9) Zhou, K.; Wang, X.; Sun, X.; Peng, Q.; Li, Y. Enhanced Catalytic Activity of Ceria Nanorods from Well-Defined Reactive Crystal Planes. *J. Catal.* **2005**, *229* (1), 206−212.

(10) Tana; Zhang, M.; Li, J.; Li, H.; Li, Y.; Shen, W. Morphology-Dependent Redox and Catalytic Properties of CeO_2 Nanostructures: Nanowires, Nanorods and Nanoparticles. *Catal. Today* **2009**, *148* (1), 179−183.

(11) Trovarelli, A. Catalytic Properties of Ceria and CeO_2-Containing Materials. *Catal. Rev.* **1996**, *38* (4), 439−520.

(12) Zhou, K.; Li, Y. Catalysis Based on Nanocrystals with Well-Defined Facets. *Angew. Chem., Int. Ed.* **2012**, *51* (3), 602−613.

(13) Mai, H.-X.; Sun, L.-D.; Zhang, Y.-W.; Si, R.; Feng, W.; Zhang, H.-P.; Liu, H.-C.; Yan, C.-H. Shape-Selective Synthesis and Oxygen Storage Behavior of Ceria Nanopolyhedra, Nanorods, and Nanocubes. *J. Phys. Chem. B* **2005**, *109* (51), 24380−24385.

(14) Agarwal, S.; Lefferts, L.; Mojet, B. L.; Ligthart, D. A. J. M.; Hensen, E. J. M.; Mitchell, D. R. G.; Erasmus, W.; Anderson, B. G.; Olivier, E. J.; Neethling, J. H.; et al. Exposed Surfaces on Shape Controlled Ceria Nanoparticles Revealed via ACTEM and Water Gas Shift Reactivity. *ChemSusChem* **2013**, *6* (10), 1898−1906.

(15) Florea, I.; Feral-Martin, C.; Majimel, J.; Ihiawakrim, D.; Hirlimann, C.; Ersen, O. Three-Dimensional Tomographic Analyses of CeO_2 Nanoparticles. *Cryst. Growth Des.* **2013**, *13* (3), 1110−1121.

(16) Liu, L.; Cao, Y.; Sun, W.; Yao, Z.; Liu, B.; Gao, F.; Dong, L. Morphology and Nanosize Effects of Ceria from Different Precursors on the Activity for NO Reduction. *Catal. Today* **2011**, *175* (1), 48−54.

(17) Wu, Z.; Li, M.; Howe, J.; Meyer, H. M.; Overbury, S. H. Probing Defect Sites on CeO_2 Nanocrystals with Well-Defined Surface Planes by Raman Spectroscopy and O_2 Adsorption. *Langmuir* **2010**, *26* (21), 16595−16606.

(18) Lee, Y.; He, G.; Akey, A. J.; Si, R.; Flytzani-Stephanopoulos, M.; Herman, I. P. Raman Analysis of Mode Softening in Nanoparticle $CeO_{2-\delta}$ and Au-$CeO_{2-\delta}$ during CO Oxidation. *J. Am. Chem. Soc.* **2011**, *133* (33), 12952−12955.

(19) Stair, P. C.; Li, C. Ultraviolet Raman spectroscopy of catalysts and other solids. *J. Vac. Sci. Technol., A* **1997**, *15*, 1679−1684.

(20) Taniguchi, T.; Watanabe, T.; Sugiyama, N.; Subramani, A. K.; Wagata, H.; Matsushita, N.; Yoshimura, M. Identifying Defects in Ceria-Based Nanocrystals by UV Resonance Raman Spectroscopy. *J. Phys. Chem. C* **2009**, *113* (46), 19789−19793.

(21) Breysse, M.; Guenin, M.; Claudel, B.; Veron, J. Catalysis of Carbon Monoxide Oxidation by Cerium Dioxide: II. Microcalorimetric Investigation of Adsorption and Catalysis. *J. Catal.* **1973**, *28* (1), 54−62.

(22) Han, W.-Q.; Wen, W.; Hanson, J. C.; Teng, X.; Marinkovic, N.; Rodriguez, J. One-Dimensional Ceria as Catalyst for the Low-Temperature Water-Gas Shift Reaction. *J. Phys. Chem. C* **2009**, *113* (52), 21949−21955.

(23) Shido, T.; Iwasawa, Y. Regulation of Reaction Intermediate by Reactant in the Water-Gas Shift Reaction on CeO_2, in Relation to Reactant-Promoted Mechanism. *J. Catal.* **1992**, *136* (2), 493−503.

(24) Agarwal, S.; Lefferts, L.; Mojet, B. L. Ceria Nanocatalysts: Shape Dependent Reactivity and Formation of OH. *ChemCatChem* **2013**, *5* (2), 479−489.

(25) Keramidas, V. G.; White, W. B. Raman Spectra of Oxides with the Fluorite Structure. *J. Chem. Phys.* **1973**, *59* (3), 1561−1562.

(26) Weber, W. H.; Hass, K. C.; McBride, J. R. Raman study of CeO_2: Second-Order Scattering, Lattice Dynamics, and Particle-Size Effects. *Phys. Rev. B* **1993**, *48* (1), 178−185.

(27) Mochizuki, S. Infrared optical Properties of Cerium Oxide. *Phys. Status Solidi B* **1982**, *114*, 189.

(28) Popović, Z. V.; Dohčević-M, Z.; Šćepanović, M.; Grujić-Brojčin, M.; Aškrabić, S. Raman Scattering on Nanomaterials and Nanostructures. *Ann. Phys. (Berlin, Ger.)* **2011**, *523* (1−2), 62−74.

(29) Kourouklis, G. A.; Jayaraman, A.; Espinosa, G. P. High-pressure Raman Study of CeO_2 to 35 GPa and Pressure-Induced Phase Transformation from the Fluorite Structure. *Phys. Rev. B* **1988**, *37* (8), 4250−4253.

(30) Bertie, J. E.; Ahmed, M. K.; Eysel, H. H. Infrared intensities of liquids. 5. Optical and Dielectric Constants, Integrated Intensities, and Dipole Moment Derivatives of Water and Water-d2 at 22 °C. *J. Phys. Chem.* **1989**, *93* (6), 2210−2218.

(31) Badri, A.; Binet, C.; Lavalley, J.-C. An FTIR Study of Surface Ceria Hydroxyl Groups During a Redox Process with H_2. *J. Chem. Soc., Faraday Trans.* **1996**, *92* (23), 4669−4673.

(32) Li, C.; Sakata, Y.; Arai, T.; Domen, K.; Maruya, K.; Onishi, T. Carbon Monoxide and Carbon Dioxide Adsorption on Cerium Oxide Studied by Fourier-Transform Infrared Spectroscopy. Part 1.-Formation of Carbonate Species on Dehydroxylated CeO_2 at Room Temperature. *J. Chem. Soc., Faraday Trans. 1* **1989**, *85* (4), 929−943.
(33) Li, C.; Sakata, Y.; Arai, T.; Domen, K.; Maruya, K.; Onishi, T. Adsorption of Carbon Monoxide and Carbon Dioxide on Cerium Oxide Studied by Fourier-Transform Infrared Spectroscopy. Part 2.-Formation of Formate Species on Partially Reduced CeO_2 at Room Temperature. *J. Chem. Soc., Faraday Trans. 1* **1989**, *85* (6), 1451−1461.
(34) Binet, C.; Badri, A.; Boutonnet-Kizling, M.; Lavalley, J.-C. FTIR Study of Carbon Monoxide Adsorption on Ceria: CO Carbonite Dianion Adsorbed Species. *J. Chem. Soc., Faraday Trans.* **1994**, *90* (7), 1023−1028.
(35) Bozon-Verduraz, F.; Bensalem, A. IR Studies of Cerium Dioxide: Influence of Impurities and Defects. *J. Chem. Soc., Faraday Trans.* **1994**, *90* (4), 653−657.
(36) Binet, C.; Badri, A.; Lavalley, J.-C. A Spectroscopic Characterization of the Reduction of Ceria from Electronic Transitions of Intrinsic Point Defects. *J. Phys. Chem.* **1994**, *98* (25), 6392−6398.
(37) Spanier, J. E.; Robinson, R. D.; Zhang, F.; Chan, S.-W.; Herman, I. P. Size-Dependent Properties of CeO_{2-y} Nanoparticles as Studied by Raman Scattering. *Phys. Rev. B* **2001**, *64* (24), 245407.
(38) Binet, C.; Daturi, M.; Lavalley, J.-C. IR Study of Polycrystalline Ceria Properties in Oxidised and Reduced States. *Catal. Today* **1999**, *50*, 207−225.
(39) Binet, C.; Jadi, A.; Lavalley, J.-C. Etude par Spectroscopie Infrarouge de l'Adsorption du Dioxyde et du Monoxyde de Carbone sur la Cerine; Influence de l'Etat de Reduction de la Cerine. *J. Chim. Phys. Phys.-Chim. Biol.* **1992**, *89*, 1779−1797.
(40) Li, C.; Domen, K.; Maruya, K.-i.; Onishi, T. Spectroscopic Identification of Adsorbed Species Derived from Adsorption and Decomposition of Formic Acid, Methanol, and Formaldehyde on Cerium Oxide. *J. Catal.* **1990**, *125* (2), 445−455.
(41) Vayssilov, G. N.; Mihaylov, M.; Petkov, P. S.; Hadjiivanov, K. I.; Neyman, K. M. Reassignment of the Vibrational Spectra of Carbonates, Formates, and Related Surface Species on Ceria: A Combined Density Functional and Infrared Spectroscopy Investigation. *J. Phys. Chem. C* **2011**, *115* (47), 23435−23454.
(42) Appel, L. G.; Eon, J. G.; Schmal, M. The CO_2−CeO_2 Interaction and its Role in the CeO_2 Reactivity. *Catal. Lett.* **1998**, *56*, 199−202.
(43) Nolan, M.; Watson, G. W. The Surface Dependence of CO Adsorption on Ceria. *J. Phys. Chem. B* **2006**, *110* (33), 16600−16606.
(44) Staudt, T.; Lykhach, Y.; Tsud, N.; Skala, T.; Prince, K. C.; Matlin, V.; Libuda, J. Electronic Structure of Magnesia-Ceria Model Catalysts, CO_2 Adsorption, and CO_2 Activation: A Synchrotron Radiation Photoelectron Spectroscopy Study. *J. Phys. Chem. C* **2011**, *115*, 8716−8724.
(45) Staudt, T.; Lykhach, Y.; Tsud, N.; Skála, T.; Prince, K. C.; Matolín, V.; Libuda, J. Ceria Reoxidation by CO_2: A Model Study. *J. Catal.* **2010**, *275*, 181−185.
(46) Jin, T.; Zhou, Y.; Mains, G. J.; White, J. M. Infrared and X-ray Photoelectron Spectroscopy Study of CO and CO_2 on Pt/CeO_2. *J. Phys. Chem.* **1987**, *91*, 5931−5937.
(47) Guenin, M. Activité Catalytique du Dioxyde de Cérium dans l'Oxydation du Monoxyde de Carbone. *Ann. Chim.* **1973**, *8* (2), 147−158.
(48) Sayle, T. X. T.; Molinari, M.; Das, S.; Bhatta, U. M.; Möbus, G.; Parker, S. C.; Seal, S.; Sayle, D. C. Environment-Mediated Structure, Surface Redox Activity and Reactivity of Ceria Nanoparticles. *Nanoscale* **2013**, *5* (13), 6063−6073.
(49) Walsh, A.; Woodley, S. M.; Catlow, C. R. A.; Sokol, A. A. Potential Energy Landscapes for Anion Frenkel-Pair Formation in Ceria and India. *Solid State Ionics* **2011**, *184* (1), 52−56.
(50) Minervini, L.; Zacate, M. O.; Grimes, R. W. Defect Cluster Formation in M_2O_3-Doped CeO_2. *Solid State Ionics* **1999**, *116* (3−4), 339−349.
(51) McBride, J. R.; Hass, K. C.; Poindexter, B. D.; Weber, W. H. Raman and X-ray Studies of $Ce_{1-x}RE_xO_{2-y}$ where RE=La, Pr, Nd, Eu, Gd, and Tb. *J. Appl. Phys.* **1994**, *76* (4), 2435−2441.
(52) Nakajima, A.; Yoshihara, A.; Ishigame, M. Defect-Induced Raman Spectra in Doped CeO_2. *Phys. Rev. B* **1994**, *50* (18), 13297−13307.
(53) Köck, E.-M.; Kogler, M.; Bielz, T.; Klötzer, B.; Penner, S. In Situ FT-IR Spectroscopic Study of CO_2 and CO Adsorption on Y_2O_3, ZrO_2, and Yttria-Stabilized ZrO_2. *J. Phys. Chem. C* **2013**, *117* (34), 17666−17673.
(54) Huang, M.; Fabris, S. CO Adsorption and Oxidation on Ceria Surfaces from DFT+U Calculations. *J. Phys. Chem. C* **2008**, *112*, 8643−8648.
(55) Dos Santos, M. L.; Lima, R. C.; Riccardi, C. S.; Tranquilin, R. L.; Bueno, P. R.; Varela, J. A.; Longo, E. Preparation and Characterization of Ceria Nanospheres by Microwave-Hydrothermal Method. *Mater. Lett.* **2008**, *62*, 4509−4511.
(56) Filtschew, A.; Stranz, D.; Hess, C. Mechanism of NO_2 Storage in Ceria Studied Using Combined In Situ Raman/FTIR Spectroscopy. *Phys. Chem. Chem. Phys.* **2013**, *15*, 9066−9069.
(57) Namai, Y.; Fukui, K.-I.; Iwasawa, Y. Atom-Resolved Noncontact Atomic Force Microscopic and Scanning Tunneling Microscopic Observations of the Structure and Dynamic Behavior of CeO2 (111) Surfaces. *Catal. Today* **2003**, *85* (2−4), 79−91.
(58) Nörenberg, H.; Briggs, G. A. D. Defect Structure of Nonstoichiometric CeO2 (111) Surfaces Studied by Scanning Tunneling Microscopy. *Phys. Rev. Lett.* **1997**, *79* (21), 4222−4225.
(59) Daniel, M.; Loridant, S. Probing Reoxidation Sites by In Situ Raman Spectroscopy: Differences Between Reduced CeO_2 and Pt/CeO_2. *J. Raman Spectrosc.* **2012**, *43* (9), 1312−1319.